

Large-Eddy Simulation of the Flow Around a Bluff Body

Siniša Krajnović* and Lars Davidson†
Chalmers University of Technology, SE-412 96 Gothenburg, Sweden

Large-eddy simulations are made of the flow around a surface-mounted cube, showing that it is possible to obtain accurate results in a coarse grid simulation. The inadequate resolution is compensated for by the use of a dynamic one-equation subgrid-scale model. Two one-equation subgrid models are used here to model the subgrid-scale stress tensor. A series of time-averaged velocities and turbulent stresses are computed and compared with the experiments and show good agreement. Global quantities such as drag and lift coefficients and vortex shedding frequency are presented. The transfer of the turbulent energy was studied and the reverse transfer of energy (backscatter) was predicted. Coherent structures and other flow features were also examined. The results showed good agreement with experimental observations.

Introduction

THE flow around a three-dimensional bluff body is of great interest in engineering practice. Typical examples of engineering applications are the computation of wind loads on buildings and simulations of the flow around vehicles. This work is connected to the latter and studies some aspects related to vehicle aerodynamics, such as drag and lift. Most studies of this kind of flow are experimental. Early studies were done by Castro and Robins¹ and Hunt et al.,² and the most recent papers are by Schofield and Logan,³ Larousse et al.,⁴ Martinuzzi and Tropea,⁵ and Hussein and Martinuzzi.⁶

The best documented experimental work on this flow is by Martinuzzi and Tropea⁵ concerning the flow around a surface-mounted cube. This flow was recently computed by Shah and Ferziger⁷ using large-eddy simulation (LES). This was the test case used at two workshops^{8,9} at which both LES and Reynolds-averaged Navier–Stokes (RANS) results were presented. Simulations were made at two Reynolds numbers, $Re = 3 \times 10^3$ and 4×10^4 . Many of these LES were done using a fine resolution (more than 10^6 nodes for the low Reynolds number case). Near the wall, these simulations approach direct numerical simulation (DNS), resolving the near-wall streaks and may be described as quasi-DNS (QDNS).¹⁰ The influence of the subgrid-scale (SGS) model is then small. Although these LES were carried out with considerable success, the extension of this kind of simulation to higher Reynolds number and more complex geometry (typical for vehicle aerodynamics) implies very high computational costs.

An interesting simulation is Iaccarino and Durbin's,¹¹ who made unsteady RANS (URANS) simulations of this flow using the v^2-f turbulent model. They reduced the spanwise length from the 7 cube heights H used in the LES to only $3H$. A computational mesh of half a million nodes was used, but the actual resolution was similar to that used in LES^{7–9} because the URANS computational domain is smaller by some 58% in the spanwise direction.

A large amount of effort was spent in the last decade to overcome the high computational cost required in wall-resolved LES. Many of the suggested modifications of LES include modeling of the near-wall region in one way or another (for example, see Refs. 12–14). Speziale¹⁵ proposed to combine URANS and very large-eddy sim-

ulation (VLES) in simulations with coarse mesh. Woodruff et al.¹⁶ demonstrated that LES can be used in coarse meshes in the absence of solid walls.

The purpose of this paper is to present LES of the flow around a surface-mounted cube at moderate Reynolds number ($Re = 4 \times 10^4$) where the SGS model plays an important role and a relatively coarse mesh is used. The inadequate resolution is compensated for by the use of a dynamic one-equation SGS model. The previous LES presented in Refs. 7–9 used the Smagorinsky,¹⁷ the dynamic Smagorinsky (see Refs. 18 and 19), the dynamic mixed Smagorinsky, and the Schuman²⁰ models. The dynamic mixed model and the Schuman model were used for low-Reynolds-number simulation only. The influence of these two SGS models was small because of the very fine resolution (524,000 and 1,152,000 nodes, respectively). The use of a coarse mesh will dramatically reduce the computational cost of the simulations described in Refs. 7–9 and hopefully still give reasonable results. Depending on the decrease in the computational cost, more challenging flows could then be simulated with LES.

Problem Statement and Computational Details

The bluff body used in this work is a sharp-edged, surface-mounted cube. The geometry of the computational domain is given in Fig. 1. The Reynolds number was $Re = U_b H / \nu = 4 \times 10^4$ based on the incoming mean bulk velocity U_b and the cube height H . The cube is located between $x/H = 0$ and 1, and the channel height is $h = 2H$ (Fig. 1). Six simulations were made with two dynamic one-equation SGS models. To assess the effect of the SGS model, we made an additional three simulations without a SGS model (NOM, NOM2, and NOM3 in Tables 1–3). To establish the results' grid independence, we made computations on three different computational grids. Details of these simulations are given in Tables 1 and 2. The computational domain had an upstream length of $x_1/H = 3$ and downstream length of $x_2/H = 6$, and the spanwise width was set to $b/H = 7$. The time step was set to 0.02 in the coarse grid simulations and 0.01 in the medium and fine grid simulations. This gave a maximum Courant–Friedrichs–Lewy (CFL) number of approximately 1.5. The CFL number was smaller than one in 98% of the cells. The influence of the temporal resolution was investigated (not shown in the paper), and it was found that a decrease in time step did not affect the results. The distance from the solid walls to the nearest grid point is denoted δ_x , δ_y , and δ_z in the x , y , and z directions, respectively (see Table 1). The grid distribution was uniform with a cell size of Δ_x close to the inlet and outlet and Δ_z close to the lateral friction-free surfaces of the channel. A geometric distribution was used to stretch the cell size between these limiting cell sizes and in the y direction.

Boundary Conditions

Instantaneous results of LES of channel flow were used as the inlet boundary condition in Refs. 7–9. This inlet boundary condition provides correct turbulent intensity and shear in the upstream

Received 4 November 2000; presented as Paper 2001-0432 at the AIAA 39th Aerospace Sciences Meeting, Reno, NV, 8–11 January 2001; revision received 3 August 2001; accepted for publication 15 November 2001. Copyright © 2002 by Siniša Krajnović and Lars Davidson. Published by the American Institute of Aeronautics and Astronautics, Inc., with permission. Copies of this paper may be made for personal or internal use, on condition that the copier pay the \$10.00 per-copy fee to the Copyright Clearance Center, Inc., 222 Rosewood Drive, Danvers, MA 01923; include the code 0001-1452/02 \$10.00 in correspondence with the CCC.

*Graduate Student, Department of Thermo and Fluid Dynamics; sinisa@tfd.chalmers.se.

†Professor, Department of Thermo and Fluid Dynamics; lada@tfd.chalmers.se.

flow. Such a boundary condition can be created for this test case because the Reynolds number is low or moderate, making LES of the channel flow feasible. In flow with higher Reynolds number, for example, the flow around a buslike body,^{21,22} it is too costly to obtain this kind of inlet boundary condition. The experimental profile (constant in time) was used at the inlet in this work. We also tried to superimpose random noise (2% of the mean statistical profile) on the mean profile. This random noise had a very harmful influence on the pressure solution, leading to high-frequency oscillations of global quantities, such as drag and lift, and was thus removed. The lateral boundaries were treated as slip surfaces using the symmetry conditions $\partial u/\partial z = \partial v/\partial z = w = 0$. At the downstream boundary, the convective boundary condition $\partial u_i/\partial t + U_c(\partial u_i/\partial x) = 0$ was used. Here, U_c was set equal to the mean bulk velocity U_b . No-slip conditions were used at the solid walls. The homogeneous Neumann condition was used for the pressure at all boundaries.

Numerical Method

An implicit finite volume method is used for solving the incompressible Navier–Stokes equations on nonstaggered grids.^{13,23,24} Both convective and viscous plus subgrid fluxes are approximated by central differences of second-order accuracy. A Crank–Nicolson second-order scheme was used for time integration. Although no explicit dissipation is added to prevent odd–even decoupling, an implicit dissipation is present. This is done by adding the difference between the pressure gradient at the face and the node. It can be shown that this term is proportional to the third derivative of pressure, that is, $\partial^3 p/\partial x_i^3$. This term corresponds to Rhie–Chow dissipation.²⁵ This implicit dissipation in combination with an implicit computational code used in this work is probably the reason for converged simulation in the no-model case. Details about this code are given in Ref. 13.

This work uses the top-hat filter. The grid filtering is applied implicitly through the discretization. The explicit filtering at the test level is done numerically by integrating over the test cell assuming linear variation of the variables,²⁶ that is (Fig. 2),

$$\begin{aligned} \bar{u}_{I,J,K} = & \frac{1}{8} \left(\bar{u}_{I-\frac{1}{2},J-\frac{1}{2},K-\frac{1}{2}} + \bar{u}_{I+\frac{1}{2},J-\frac{1}{2},K-\frac{1}{2}} \right. \\ & + \bar{u}_{I-\frac{1}{2},J+\frac{1}{2},K-\frac{1}{2}} + \bar{u}_{I+\frac{1}{2},J+\frac{1}{2},K-\frac{1}{2}} \\ & + \bar{u}_{I-\frac{1}{2},J-\frac{1}{2},K+\frac{1}{2}} + \bar{u}_{I+\frac{1}{2},J-\frac{1}{2},K+\frac{1}{2}} \\ & \left. + \bar{u}_{I-\frac{1}{2},J+\frac{1}{2},K+\frac{1}{2}} + \bar{u}_{I+\frac{1}{2},J+\frac{1}{2},K+\frac{1}{2}} \right) \end{aligned} \quad (1)$$

An overbar denotes a grid filter with filter width Δ , and $\bar{\cdot}$ is a test filter with filter width $\Delta = 2\Delta$.

Governing Equations and SGS Modeling

In LES, the contribution of the large, energy-carrying scales to momentum and energy transfer is computed exactly, and only the effect of the smallest scales of the turbulence is modeled.

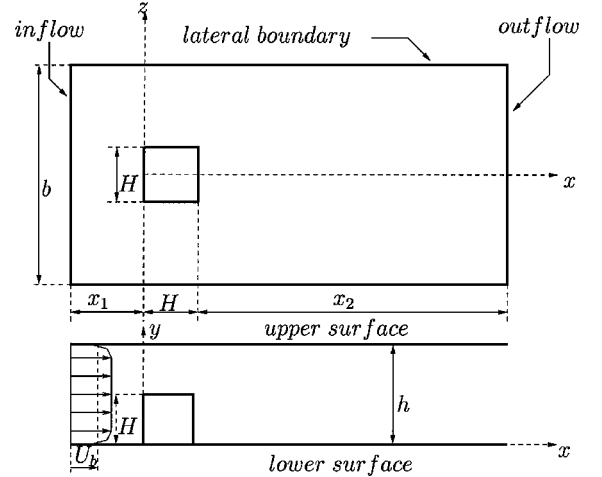


Fig. 1 Geometry of the computational domain.

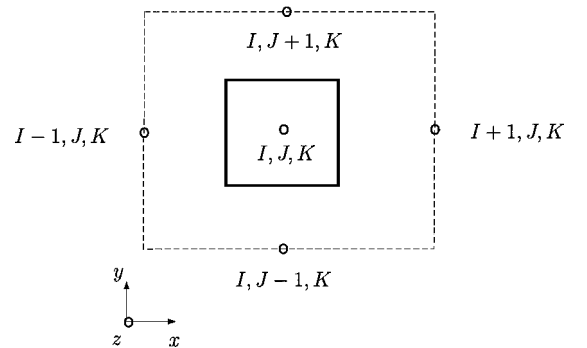


Fig. 2 Grid filtering volume (—) and test filtering volume (- - -).

Table 1 Summary of simulations

Case	N_x^a	N_y^b	N_z^c	δ_x	δ_y	δ_z	Δ_x	Δ_z
OEM	16	24	16	0.048	0.023	0.078	0.20	0.20
LDKM	16	24	16	0.048	0.023	0.078	0.20	0.20
NOM	16	24	16	0.048	0.023	0.078	0.20	0.20
OEM2	24	32	32	0.023	0.014	0.029	0.10	0.135
LDKM2	24	32	32	0.023	0.014	0.029	0.10	0.135
NOM2	24	32	32	0.023	0.014	0.029	0.10	0.135
OEM3	40	32	48	0.024	0.014	0.020	0.083	0.135
LDKM3	40	32	48	0.024	0.014	0.020	0.083	0.135
NOM3	40	32	48	0.024	0.014	0.020	0.083	0.135

^aNumber of points on the surface of the cube in the streamwise direction.

^bNumber of points on the surface of the cube in the y direction.

^cNumber of points on the surface of the cube in the spanwise direction.

Table 2 Lengths for reattachment, X_{R1} , and separation, X_{F1} , as well as vortex shedding frequency Sr from the lateral walls

Contribution	Model	Grid	X_{F1}	X_{R1}	Sr
Martinuzzi and Tropea ⁵	Experiment	—	1.04	1.61	0.145
OEM	OEM	$82 \times 50 \times 66$	0.970	1.380	0.134
LDKM	LDKM	$82 \times 50 \times 66$	0.944	1.413	0.115
NOM	—	$82 \times 50 \times 66$	0.339	1.887	0.092
OEM2	OEM	$162 \times 66 \times 98$	1.115	1.454	0.119
LDKM2	LDKM	$162 \times 66 \times 98$	1.090	1.544	0.092
NOM2	—	$162 \times 66 \times 98$	0.560	2.210	0.100
OEM3	OEM	$210 \times 66 \times 114$	1.100	1.453	0.146
LDKM3	LDKM	$210 \times 66 \times 114$	1.135	1.443	0.115
NOM3	—	$210 \times 66 \times 114$	0.711	1.746	0.111
Shah and Ferziger ⁷	Smagorinsky	$192 \times 64 \times 96$	1.050	1.650	—
Breuer et al. (see Refs. 9 and 46)	Smagorinsky	$165 \times 65 \times 97$	1.287	1.696	—
Breuer et al. (see Refs. 9 and 46)	Dynamic	$165 \times 65 \times 97$	0.998	1.432	—
Wengle (see Refs. 9 and 46)	Smagorinsky	$144 \times 58 \times 88$	0.808	1.722	—
Iaccarino and Durbin ¹¹	RANS	500,000 ($b = 3H$)	0.640	3.315	—
Iaccarino and Durbin ¹¹	URANS	500,000 ($b = 3H$)	0.732	1.876	0.17

Table 3 Mean and rms values of drag and lift coefficients

Case	$\langle C_D \rangle_t$	$C_{D,rms}$	$\langle C_L \rangle_t$	$C_{L,rms}$
OEM	1.140	0.062	0.920	0.038
LDKM	1.160	0.070	0.910	0.040
NOM	1.244	0.051	0.837	0.032
OEM2	1.179	0.055	1.217	0.038
LDKM2	1.171	0.057	1.206	0.043
NOM2	1.240	0.041	1.101	0.052
OEM3	1.166	0.047	1.119	0.038
LDKM3	1.148	0.051	1.099	0.041
NOM3	1.224	0.051	1.099	0.040

Decomposition into a large-scale component and a small SGS is done by applying a filtering operation,

$$\bar{f}(x_i) = \int_{\Omega} f(x'_i) G(x_i, x'_i) dx'_i \quad (2)$$

where G is the filter function and Ω is the entire flow domain. A top-hat filter with filter function $G = (1/\Delta)H(\frac{1}{2}\Delta - |x - x'|)$, where $H(x)$ is the Heaviside function, is used in this work. The filter width Δ is defined as $\Delta = (\Delta_1 \Delta_2 \Delta_3)^{1/3}$, where Δ_i are the computational mesh sizes in each coordinate directions. Filtering the Navier–Stokes and the continuity equations gives the governing equations

$$\frac{\partial \bar{u}_i}{\partial t} + \frac{\partial}{\partial x_j} (\bar{u}_i \bar{u}_j) = -\frac{1}{\rho} \frac{\partial \bar{p}}{\partial x_i} + \nu \frac{\partial^2 \bar{u}_i}{\partial x_j \partial x_j} - \frac{\partial \tau_{ij}}{\partial x_j} \quad (3)$$

$$\frac{\partial \bar{u}_i}{\partial x_i} = 0 \quad (4)$$

Note that the derivation of Eqs. (3) and (4) from the Navier–Stokes equations, the continuity equation, and Eq. (2) requires that the differentiation operations commute with the filtering operator, that is,

$$\frac{\partial \bar{f}}{\partial x_i} = \bar{\frac{\partial f}{\partial x_i}} \quad (5)$$

The commutation property in Eq. (5) is valid if the filter width Δ is constant. However, a variable filter width is used in inhomogeneous flow (including the flow studied in this paper). That results in a violation of Eq. (5). An analysis of the commutation error²⁷ shows that the error is of order $\mathcal{O}(\Delta^2)$, and thus, in this work it is of the same order as the discretization error.

The effect of the small scales appears in the SGS stress tensor, $\tau_{ij} = \overline{u_i u_j} - \bar{u}_i \bar{u}_j$, which must be modeled. Two one-equation sub-grid models are used in the present study. Both models are SGS kinetic energy models. The SGS stress tensor is modeled as $\tau_{ij} = -2\nu_{sgs} \bar{S}_{ij}$ with the eddy viscosity defined as $\nu_{sgs} = C \Delta k_{sgs}^{1/2}$ and SGS kinetic energy as $k_{sgs} = 1/2 \tau_{ii}$.

The first model was developed by Davidson²⁸ [dynamic one-equation model (OEM)] and has been successfully applied to fully developed channel flow²⁹ and vortex shedding flow around square cylinders.^{30,31} The modeled transport equation for the sub-grid kinetic energy k_{sgs} reads

$$\begin{aligned} \frac{\partial k_{sgs}}{\partial t} + \frac{\partial}{\partial x_j} (\bar{u}_j k_{sgs}) &= \Pi_{k_{sgs}} \\ &+ \frac{\partial}{\partial x_j} \left[\left(C_{hom} \Delta k_{sgs}^{\frac{1}{2}} + \nu \right) \frac{\partial k_{sgs}}{\partial x_j} \right] - C_* \frac{k_{sgs}^{\frac{3}{2}}}{\Delta} \end{aligned} \quad (6)$$

The first term on the right-hand side is the SGS dissipation of the resolved kinetic energy and is defined as $\Pi_{k_{sgs}} = 2C \Delta k_{sgs}^{1/2} \bar{S}_{ij} \bar{S}_{ij}$. C_{hom} [see Eq. (8)] is a constant value of the dynamic coefficient C in space, and C_* [see Eq. (10)] is the dissipation coefficient. The dynamic coefficient C is computed as

$$C = -\frac{\mathcal{L}_{ij} M_{ij}}{2M_{ij} M_{ij}} \quad (7)$$

where

$$M_{ij} = \widehat{\Delta} K^{\frac{1}{2}} \widehat{S}_{ij} - \Delta k_{sgs}^{\frac{1}{2}} \widehat{S}_{ij}, \quad K = \widehat{k}_{sgs} + \frac{1}{2} \mathcal{L}_{ii}$$

where \mathcal{L}_{ij} are the dynamic Leonard stresses and are defined as $\mathcal{L}_{ij} = \overline{\bar{u}_i \bar{u}_j} - \bar{u}_i \bar{u}_j$. $K \equiv 1/2 T_{ii}$ is the subgrid kinetic energy on the test level, and $T_{ij} = \overline{\bar{u}_i \bar{u}_j} - \bar{u}_i \bar{u}_j$ is the SGS stress on the test level. \bar{S}_{ij} is the strain rate tensor on the grid level. A constant value of C in space, C_{hom} , is used in the momentum equations and in the diffusion term in Eq. (6). The reason for using a homogeneous coefficient is that the local coefficient C yields a highly oscillating eddy viscosity field including a significant partition with negative values, which is destabilizing in numerical simulations. C_{hom} is computed with the requirement that the SGS dissipation of the resolved kinetic energy $\Pi_{k_{sgs}}$ in the whole computational domain remains the same as it is with the local coefficient C , that is,

$$\left\langle 2C \Delta k_{sgs}^{\frac{1}{2}} \bar{S}_{ij} \bar{S}_{ij} \right\rangle_{xyz} = 2C_{hom} \left\langle \Delta k_{sgs}^{\frac{1}{2}} \bar{S}_{ij} \bar{S}_{ij} \right\rangle_{xyz} \quad (8)$$

where $\langle \rangle_{xyz}$ denotes space averaging over the entire domain.

The Smagorinsky model¹⁷ is based on the assumption of local equilibrium of SGS turbulent kinetic energy k_{sgs} , that is $\Pi_{k_{sgs}} - \varepsilon_{k_{sgs}} = 0$, where $\varepsilon_{k_{sgs}}$ is the dissipation of k_{sgs} . A slightly better assumption for estimating the coefficient C_* in the dissipation term, would be to assume that the filtered right-hand side of the k_{sgs} equation is equal to that of the K equation, that is,

$$\widehat{\Pi}_{k_{sgs}} - C_* \left(\widehat{k_{sgs}^{\frac{3}{2}}} / \widehat{\Delta} \right) = \Pi_K - C_* \left(K^{\frac{3}{2}} / \widehat{\Delta} \right) \quad (9)$$

This gives the coefficient C_* in the dissipation term, for time step $n+1$,

$$C_*^{n+1} = \left[\Pi_K - \widehat{\Pi}_{k_{sgs}} + (1/\Delta) C_*^n \widehat{k_{sgs}^{\frac{3}{2}}} \right] (\widehat{\Delta} / K^{\frac{3}{2}}) \quad (10)$$

with

$$\Pi_K = 2C \widehat{\Delta} K^{\frac{1}{2}} \widehat{S}_{ij} \widehat{S}_{ij} \quad (11)$$

Note that C_*^n has been kept inside the filtering process. All local dynamic information is included through the source terms. This is physically more sound because large local variations in C appear only in the source term and the effect of the large fluctuations in the dynamic coefficients will be smoothed out. The coefficients in the one-equation model affect the stresses in only an indirect way. In the dynamic Smagorinsky model (see Refs. 18 and 19), the C coefficient is linearly proportional to the stresses, which makes it numerically unstable.

The second model studied in this paper is the localized dynamic k_{sgs} equation model (LDKM) proposed by Menon and Kim.³² The following transport equation is solved in the LDKM:

$$\begin{aligned} \frac{\partial k_{sgs}}{\partial t} + \frac{\partial}{\partial x_j} (\bar{u}_j k_{sgs}) &= \Pi_{k_{sgs}} \\ &+ \frac{\partial}{\partial x_j} \left[\left(C \Delta k_{sgs}^{\frac{1}{2}} + \nu \right) \frac{\partial k_{sgs}}{\partial x_j} \right] - C_* \frac{k_{sgs}^{\frac{3}{2}}}{\Delta} \end{aligned} \quad (12)$$

where

$$C = \frac{1}{2} \frac{\mathcal{L}_{ij} \sigma_{ij}}{\sigma_{ij} \sigma_{ij}}, \quad \sigma_{ij} = -\widehat{\Delta} k_{test}^{\frac{1}{2}} \widehat{S}_{ij}, \quad k_{test} = \frac{1}{2} \mathcal{L}_{ii} \quad (13)$$

$$C_* = \frac{\widehat{\Delta}}{k_{test}^{\frac{3}{2}}} (\nu + \nu_{sgs}) \left(\frac{\partial \bar{u}_i}{\partial x_j} \frac{\partial \bar{u}_i}{\partial x_j} - \frac{\partial \bar{u}_i}{\partial x_j} \frac{\partial \bar{u}_i}{\partial x_j} \right) \quad (14)$$

One-equation SGS models offer a number of advantages over the dynamic Smagorinsky model (see Refs. 18 and 19).

1) One-equation models can predict backscattering. In the dynamic Smagorinsky model (see Refs. 18 and 19), the dynamic coefficient must be averaged in some homogeneous direction or be clipped in an ad hoc manner. This averaging and clipping often implies that $\nu + \nu_{sgs} \geq 0$, that is, $\Pi_{k_{sgs}} \geq -2\nu \bar{S}_{ij} \bar{S}_{ij}$. Thus, the backscattering is restricted.

2) Although it is necessary to solve an additional transport equation, one-equation models are often computationally cheaper than the dynamic Smagorinsky model (see Refs. 18 and 19) because of greater numerical stability.^{30,33}

Although the two SGS models appear similar, there are some significant differences. The LDKM uses local dynamic coefficient C , whereas the OEM requires some volume averaging of this coefficient. In the OEM, similarity assumptions are made between the grid level (length scale $\ell < \Delta$, velocity scale $k_{\text{sgs}}^{1/2}$) and the test level (length scale $\ell < \Delta$, velocity scale $K^{1/2}$). However, in the LDKM, the similarity assumption is made between the grid level and the intermediate level (length scale $\Delta < \ell < \widehat{\Delta}$, velocity scale $[0.5\mathcal{L}_{kk}]^{1/2}$). The denominator in Eq. (13), $\sigma_{ij}\sigma_{ij}$, does not tend toward zero as much as the denominator, $M_{ij}M_{ij}$, in the OEM [Eq. (7)], which explains why C does not oscillate as much in the LDKM (see Ref. 34).

Results

Statistics of the Mean Flow

A series of time-averaged resolved velocities and turbulent stresses are computed and compared with the experiments. We eval-

uated the results for most of the positions measured in Ref. 5. We concentrate in this paper on the results downstream of the front edge of the cube, where the effect of the model is expected to be pronounced. The results for the velocities are generally in much better agreement with the experiment than are the results for the stresses. Some results are shown in Fig. 3. Results for other positions are presented in Ref. 35. Numerical wiggles are present in the mean velocity profile $\langle \bar{u} \rangle_t$ for $x/H = -1.0$ (see Ref. 34) because of a combination of coarse mesh in that part of the domain and the use of the central differencing scheme. As can be seen, the predictions made without a model give poor agreement, whereas the two subgrid models give good agreement with experiments. The separation region at the top of the cube without a model is much too thin (Fig. 3). This is probably because, without a model, the resolved fluctuations are not damped by any subgrid viscosity, and the resolved fluctuations consequently become too large. This gives excessively large

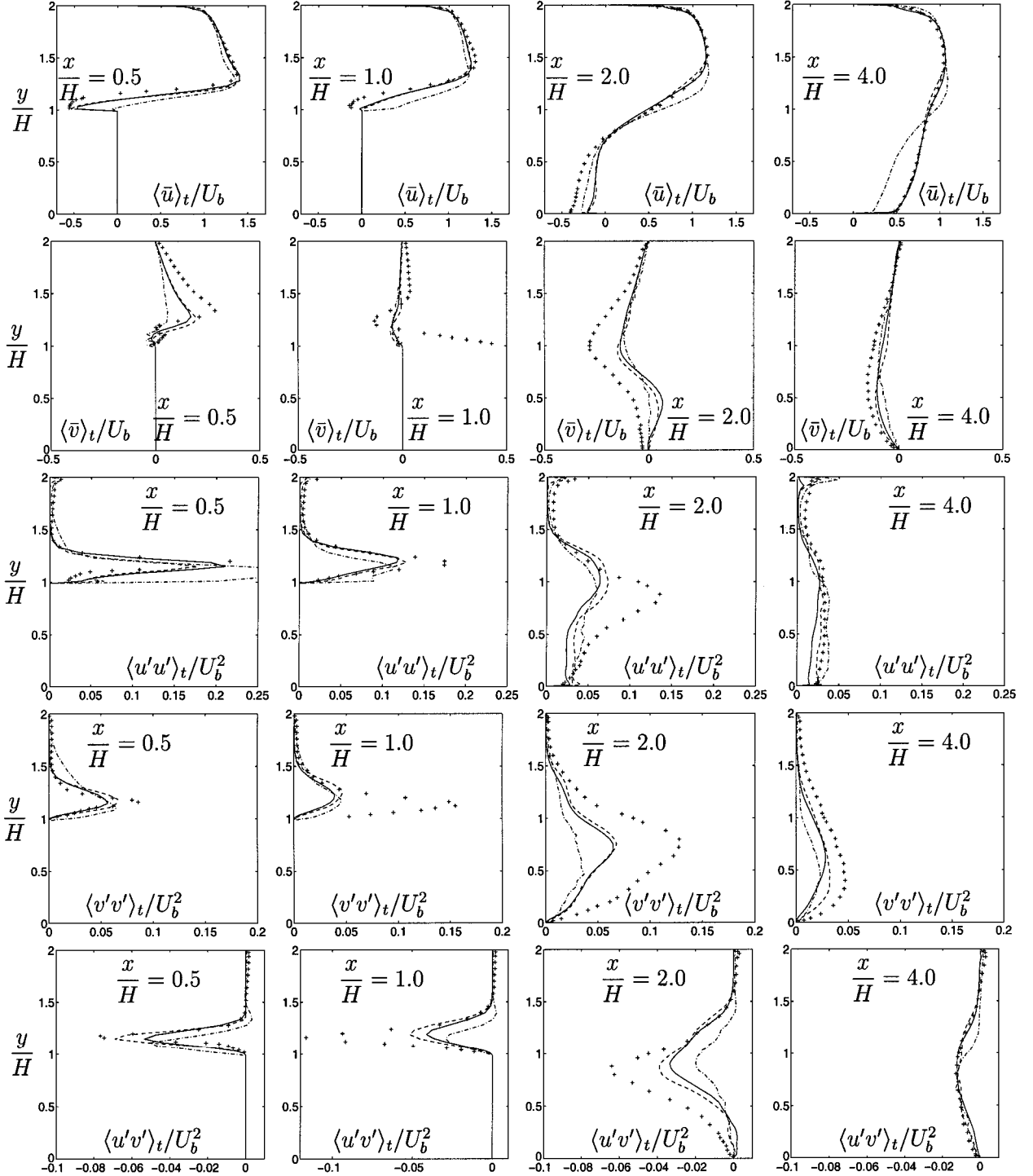


Fig. 3 Comparison between LDKM (---), OEM (—), calculation without a model (-.-), and experiments⁵ (+).

turbulent diffusion, making the separation region smaller and thinner. It can be seen in Fig. 3 that the resolved shear stress $\langle u'v' \rangle_t$ is not larger without a model than that obtained with a model; however, care should be taken in comparing these because the time-averaged velocity fields are very different. Instead, we could argue as follows: The resolved shear stress without a model is of approximately the same magnitude as with a model, although the velocity gradient of the time-averaged velocity field without a model is much smaller; thus, when the difference in the time velocity fields is taken into account, the resolved shear stress without a model is indeed larger. The two one-equation models gave similar results, but the results obtained with the LDKM are slightly better. The LDKM is local and capable of predicting the shear layer close to the upper wall of the channel. (See $\langle u'u' \rangle_t / U_b^2$ in Figs. 3 and 4.) We also computed $\langle u'^2 \rangle_t + \langle \tau_{11} \rangle_t$, $\langle v'^2 \rangle_t + \langle \tau_{22} \rangle_t$, and $\langle w'^2 \rangle_t + \langle \tau_{33} \rangle_t$ and compared them with the

experiments. The total, that is, resolved plus SGS, turbulent stresses are not shown here because we found that the differences between these and the resolved mean turbulent stresses are almost negligible.

The effect of the models is noticeable in a comparison with the calculation made without a model. These differences are especially visible close to the roof of the cube and far downstream. The case studied in this paper was a test case at the 6th ERCOFTAC/IAHR/COST Workshop⁸ using RANS models. The velocity profiles, especially farther downstream of the cube, are much better predicted by LES in the present work. The turbulent stresses are in significantly better agreement with the experimental values.

Influence of the Resolution and SGS Model

The number of grid points in medium and coarse grid simulations was chosen to be close to those in the simulations described in

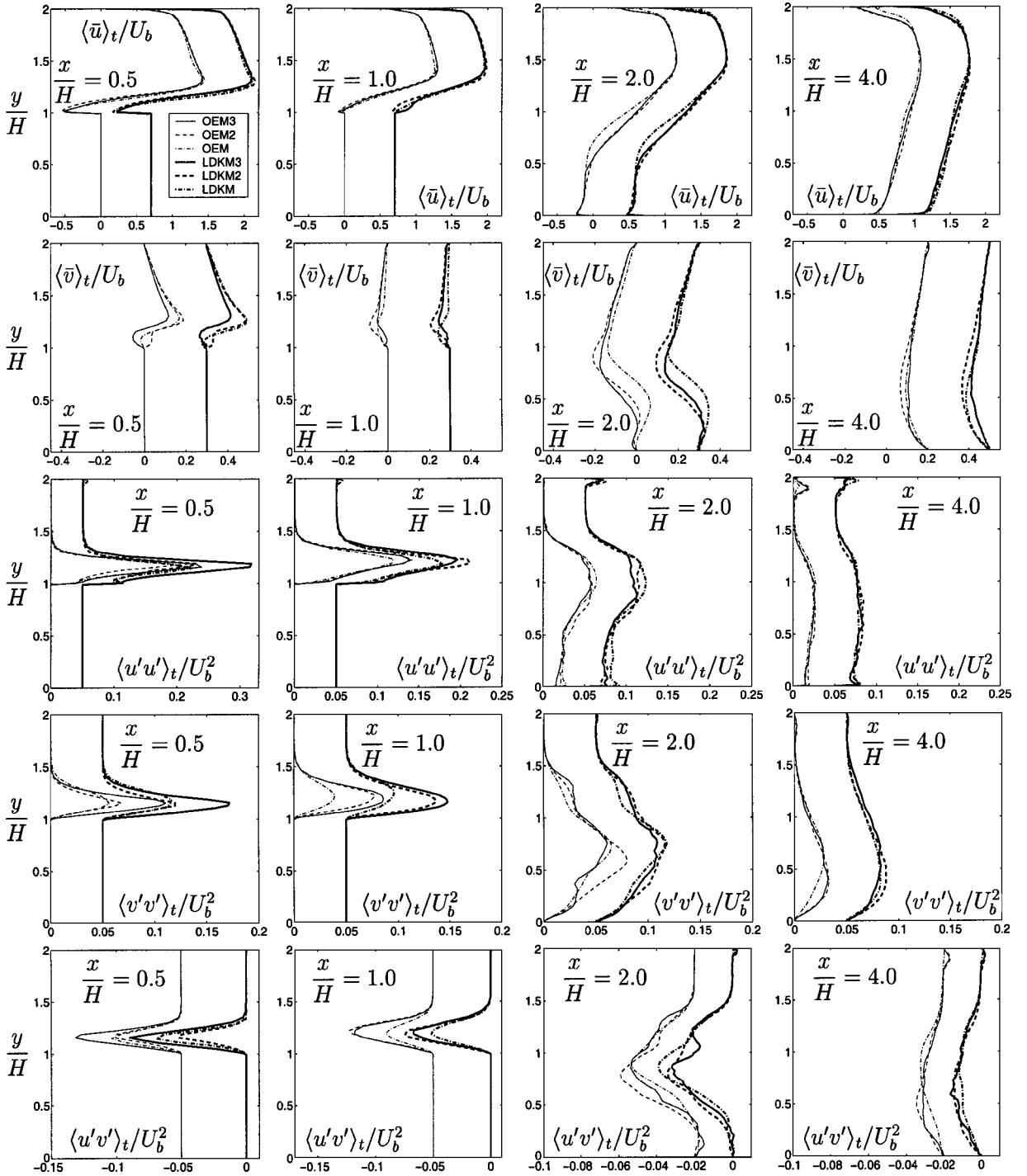


Fig. 4 Comparison of simulations on different grids.

Refs. 7–9. The grid was refined proportionally in all directions in the medium grid simulations as compared to the coarse grid simulations, whereas the refinement in the fine grid simulations is concentrated around the cube. An overview of the simulations made is given in Tables 1–3. The reattachment length X_{R1} behind the cube and the separation length X_{F1} upstream the cube are determined from the distribution of the skin-friction coefficient, $C_f = 2(\tau_w)_t / \rho U_b$, on the channel floor. Table 2 shows comparisons of different time-averaged recirculation lengths with experiments. Grid refinement has a greater effect on the separation length X_{F1} than the reattachment length X_{R1} . The best agreement with the experiments for the reattachment length is found in the medium mesh simulations. The local resolution at the position of the reattachment was lower in the fine mesh simulations than in the medium grid simulations. It appears that the local resolution is more important for the prediction of the reattachment length than is the resolution of the boundary layer on the top of the cube, which was much finer in the fine mesh simulations (Tables 1 and 2). Simulations made without a model show a far too short separation length X_{F1} and far too long reattachment length X_{R1} . Table 2 includes a comparison of the present simulations with some previous LES^{7–9} and RANS simulations.¹¹ We find that the results for X_{F1} and X_{R1} in the present simulations are comparable to the results of previous LES.^{7–9} All LES give results that are in much better agreement with experiments than RANS simulations.

The side force signal was Fourier transformed, and a peak is found in the spectrum. The Strouhal number St of this periodic component is also given in Table 2. The fine mesh resolution gives the best agreement with the experimental value of Strouhal number. The coarse grid simulation using the OEM gives a Strouhal number of 0.134 as compared to the experimental value of 0.145. No shedding frequency was reported in previous LES,⁷ whereas the shedding period corresponding to a Strouhal number of 0.17 was observed in the unsteady RANS simulation by Iaccarino and Durbin.¹¹ No vortex shedding is observed for the shear layer separating from the roof of the cube, and no peak is found in the Fourier-transformed signals of C_D and C_L . This agrees with unsteady RANS results by Iaccarino and Durbin.¹¹

The mean and rms drag and lift coefficients are given in Table 3. We know of no experimental values for drag and lift coefficients. The values of mean and rms values for the OEM and the LDKM on the coarse grid are very similar. There is a 5–9% difference in the mean drag coefficient and up to an 11% difference in the mean lift coefficient between simulations with and without SGS models. The rms values of drag and lift coefficients vary by some 40% between simulations made with and without SGS models. The impact of the grid resolution on the lift coefficients is much larger than on the drag coefficients (Table 3). This is in agreement with observations found on vortex shedding around a square cylinder.^{30,31,36}

Accuracy of the numerical results in this paper is judged from the grid refinement study. There is some 20% difference in the mean velocity profiles $\langle \bar{u} \rangle_t$ between the simulations using the coarse and fine grids at $x/H = 2.0$ (Fig. 4). This difference reduces to only 1–3% in the rest of the domain. We find very small differences between the mean velocity profiles $\langle \bar{u} \rangle_t$ using the medium and the fine grid (Fig. 4). The grid refinement leads to a decrease in the oscillations of the mean velocity field upstream of the cube, as expected (not shown in this paper). The numerical accuracy of the mean velocity profile $\langle \bar{v} \rangle_t$ is worse than that for $\langle \bar{u} \rangle_t$. The largest differences between the simulations appear in the stresses on the top of the cube. (See $x/H = 0.5$ and 1.0 in Fig. 4.) The reattachment length X_{R1} changes 1–13% (OEM) and 4–15% (LDKM) between different grid simulations. The similar difference for the separation length X_{F1} is up to an 5% in OEM and 8–9% in LDKM (Table 2). There is 2–8% difference in the mean drag coefficient $\langle C_D \rangle_t$ between the coarse and the fine grid simulations (Table 3). The corresponding difference for the mean lift coefficient $\langle C_L \rangle_t$ is 20%. Note that grid refinement does not automatically lead to better results. Contrary to expectation, we find that the agreement of some results with experiments is better on the medium grid than on the fine one. Similar results were also found in circular cylinder LES made by Breuer.³⁷

SGS Dissipation of the Resolved Kinetic Energy

Most commonly used SGS models, that is, the Smagorinsky model¹⁷ and the dynamic model of Germano (see Refs. 18 and 19), are able to account for properly the net energy flux from the resolved to the SGSs. It is well known that, in addition to this forward transport of the turbulent energy, reverse transport is also possible (backscatter). Piomelli et al.³⁸ and Domaradzki et al.³⁹ studied DNS of turbulent and transitional flows and showed that the backscatter is comparable and often larger than the net SGS dissipation. In the Smagorinsky model,¹⁷ the SGS dissipation of the resolved kinetic energy \bar{k} is $\Pi_{k_{sgs}} = -\tau_{ij} \bar{S}_{ij} \geq 0$, that is, the model is purely dissipative. This is also the case for the Germano model (see Refs. 18 and 19) because of averaging and clipping of the dynamic coefficient, as mentioned earlier. Only a few of the SGS models used today are capable of mimicking backscatter. The mixed model^{26,40} and one-equation models^{20,41,42} are probably the best known of this class of models. We refer to Refs. 39 and 43 for further discussions of the importance of backscatter and the ability of various SGS models to model this reverse transfer of turbulent energy.

Both one-equation models used in this work are able to predict a negative SGS dissipation of \bar{k} , indicating backscatter. Backscatter can be of importance, depending on how large a fraction of the total energy transport is contained in the reverse transport. The coefficient C in the model for the SGS dissipation of \bar{k} is permitted to be negative in both the OEM and the LDKM. When C becomes negative, it represents modeled backscatter. The SGS dissipation of \bar{k} , $\Pi_{k_{sgs}}$, was studied instantaneously and in the mean.³⁴ The LDKM gives a smaller magnitude of negative $\Pi_{k_{sgs}}$ than does the OEM. The strongest backscatter occurs near the front vertical corners of the cube.³⁴ It was also found in simulations by Sohankar et al.^{30,31} of the flow around a square cylinder that strong backscatter occurs near the front corners. In the flow around the cube, the lower values of negative $\Pi_{k_{sgs}}$ follow a horseshoe vortex in the case of the OEM. It was found that the LDKM predicts backscatter far upstream of the cube in regions where the grid is refined. Thus, the LDKM seems to be more sensitive to grid refinement than the OEM. This is because the LDKM is more local than the OEM. To identify the reasons for the existence of a negative $\Pi_{k_{sgs}}$, we computed the numerator in the expression of C in Eq. (7), $\langle -\mathcal{L}_{ij} M_{ij} \rangle_t$, in the position of the strongest backscatter. It is seen in Fig. 5a that $\langle -\mathcal{L}_{12} M_{12} \rangle_t$ and $\langle -\mathcal{L}_{13} M_{13} \rangle_t$ are the dominant terms in the regions of strongest negative $\langle \Pi_{k_{sgs}} \rangle_t$. \mathcal{L}_{13} is the most important negative term, as is shown in Fig. 5b. Additional results and discussion on the backscatter in this flow are provided in Ref. 34.

Flow Features

The flow patterns around a cube were sketched first by Hunt et al.² They used the information derived from visualization of the flow by smoke, hydrogen bubbles, dye, etc. A similar picture of this flow was sketched by Larousse et al.⁴ and Martinuzzi and Tropea⁵ with the support of their laser Doppler anemometer velocity measurements (Fig. 6a). We calculated vortex cores using EnSight postprocessing software and according to algorithms based on techniques outlined by Sujudi and Haimes.⁴⁴ Core segments are then used as emitters of the ribbon traces shown in Fig. 6. Note that the vortex cores in Figs. 6b–6d are plotted for the same value of vortex core strength. All of the main features of this flow observed in Refs. 2, 4, and 5 are visible in Fig. 6. These are the horseshoe vortex H, lateral vortices L, the vortex on the top of the cube T, and two recirculation vortices behind the cube W. Two simulations using one-equation models (Figs. 6b and 6c) give a similar picture of these coherent structures, in good agreement with kinematic and experimental results (Fig. 6a). The no-model simulation (Fig. 6d) gives lateral vortices that are much too short. When no model is used, the vortex on the roof of the cube is located closer to the leading edge than in the two simulations using one-equation models. The technique used for the prediction of vortex cores failed to find a horseshoe vortex in the simulation made without a model (Fig. 6d). Additional visualizations of these features can be found in Ref. 34. The two corner vortices behind the cube join in the plane of symmetry, forming an arch.³⁴ This confirms the findings in the experiments.^{2,4,5}

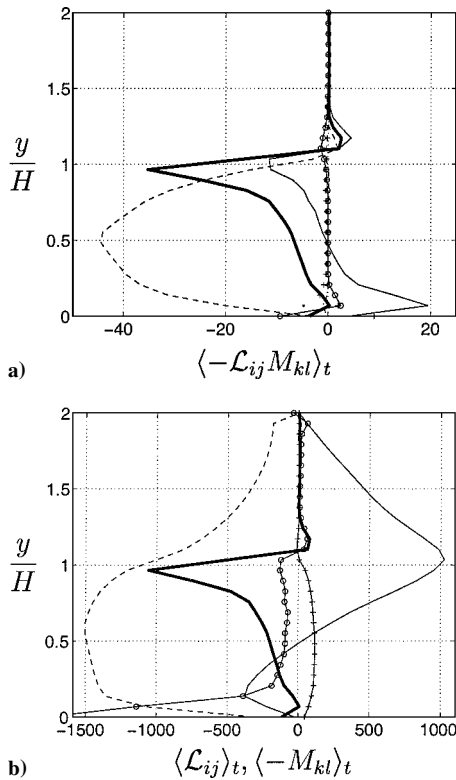


Fig. 5 OEM, $x/H = -0.2$ and $z/H = 0.6$: a) —, $\langle \Pi_{k_{sgs}} \rangle_t / 300$; —, $\langle -\mathcal{L}_{12}M_{12} \rangle_t$; ---, $\langle -\mathcal{L}_{13}M_{13} \rangle_t$; ···, $\langle -\mathcal{L}_{11}M_{11} \rangle_t$; - - - , $\langle -\mathcal{L}_{22}M_{22} \rangle_t$; ○, $\langle -\mathcal{L}_{23}M_{23} \rangle_t$; and +, $\langle -\mathcal{L}_{33}M_{33} \rangle_t$; and b) —, $\langle \Pi_{k_{sgs}} \rangle_t / 10$; —, $\langle \mathcal{L}_{12} \rangle_t$; ---, $\langle \mathcal{L}_{13} \rangle_t$; ○, $\langle -M_{12} \rangle_t / 3$; and +, $\langle -M_{13} \rangle_t$.

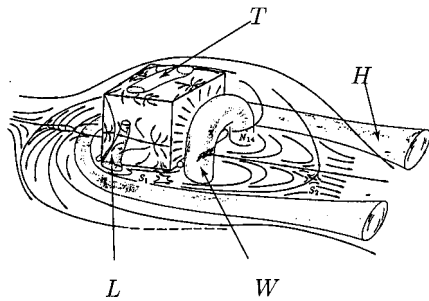


Fig. 6a Schematic representation of the flow features by Martinuzzi and Tropea (from Ref. 6 with permission).

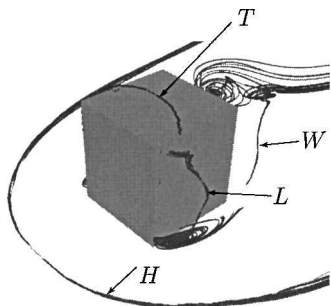


Fig. 6b Ribbon traces emitted from cores of the vortices around the cube, OEM.

We find that the location of the horseshoe vortex varies from $z/H \approx 1.7$ at $x/H = 1.75$ to $z/H \approx 0.97$ at $x/H = 5.3$ (Ref. 34). In the experiment, the position of the horseshoe leg varied from $z/H \approx 1.25$ at $x/H = 1.75$ to $z/H \approx 0.95$ at $x/H = 5.3$ (Refs. 5 and 4). To explain this difference in the location of the horseshoe legs we refer to findings by Martinuzzi and Tropea.⁵ They found that the shape of the horseshoe vortex is influenced by the oncoming boundary layer. As already mentioned, we used the experimental velocity profile (constant in time) as the inlet boundary condition. Most likely, only a real, fully developed channel flow inlet boundary condition can give the correct boundary-layer thickness. Note that

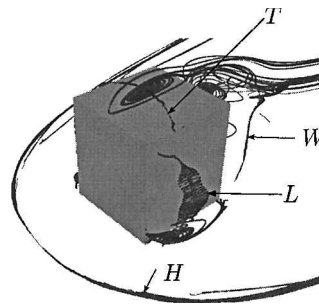


Fig. 6c Ribbon traces emitted from cores of the vortices around the cube, LDKM.

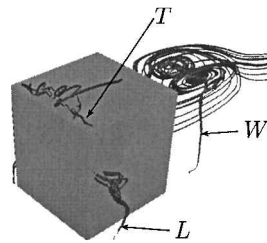


Fig. 6d Ribbon traces emitted from cores of the vortices around the cube, without a model.

in that case the resolution of the boundary layer would have to be very fine ($\Delta z^+ \leq 20$). This would correspond to a QDNS.

In Fig. 7, the oil-film visualization by Martinuzzi and Tropea⁵ is compared with streamlines projected onto the floor. Note that the streamlines in Figs. 7b–7d are emitted from the same positions in the flow. The predicted streamline pictures show most of the details observed in the experiments. In the experiments, Martinuzzi and Tropea observed three main curves in front of the cube. Curve A corresponds to the primary, upstream separation curve and curve B to the approximate time-averaged location of the horseshoe vortex. Curve C indicates a secondary recirculation at the front base of the cube.⁵ Curves A and C are clearly visible in the picture of the predicted streamlines, whereas curve B is somewhat weaker. The uncertainty of the experiment in this region is very large, and the flow between curves A and B is unstable. From this we conclude that it is not clear whether experiments or LES give the most truthful results in this part of the domain. The contour of the recirculation downstream of the cube is also clearly visible. The saddle points on the channel floor adjacent to the cube trailing-edge corners (shown as S_1 in Fig. 7a) can be observed in both simulations with the one-equation models. The other pair of saddle points on the channel floor along the reattachment line (shown as S_2 in Fig. 7a) was found only in LES with LDKM (Fig. 7c). The position of saddle points S_2 in LES with LDKM was measured to be $x/H \approx 2.3$, $z/H \approx 0.5$, as compared to the experimental $x/H \approx 2.4$, $z/H \approx 0.5$. Because of the inability to average over statistically equivalent points, the symmetry was used as a measure of whether the simulation was run for a sufficiently long time. The averaging time in the simulation was $tH/U_b = 300$ (15,000 time steps). As can be seen in Fig. 7, the surface streamlines downstream the cube are approximately symmetric, which indicates that the number of averaging samples is sufficient.

Figure 8 compares the streamlines in the symmetry plane resulting from LES with experiments.⁵ Note that the streamlines in Figs. 8b–8d are emitted from the same positions in the flow. The vortices on the top and behind the cube and the head of the horseshoe are clearly visible in simulations using one-equation models (Figs. 8b and 8c). Figures 8b and 8c are in good agreement with the experimental results in Fig. 8a. The main difference between experiment and LES result is in the position of the head of the horseshoe vortex. Similar observation was made in previous LES.⁹ The mean flow does not reattach on the top side of the cube (Figs. 8b and 8c) in the simulations with one-equation models. This agrees with experimental findings (Fig. 8a) (Refs. 6 and 45) and previous LES.⁷ A half-saddle was observed at a height of $0.72H$ on the front face of the cube as compared to the experimental height of $0.76H$ (Ref. 4). A free saddle point above the trailing edge observed in Refs. 4 and 5 is seen in both simulations using one-equations models in Figs. 8b and 8c. There is a substantial difference between the no-model prediction in Fig. 8d and the experimental results in Fig. 8a.

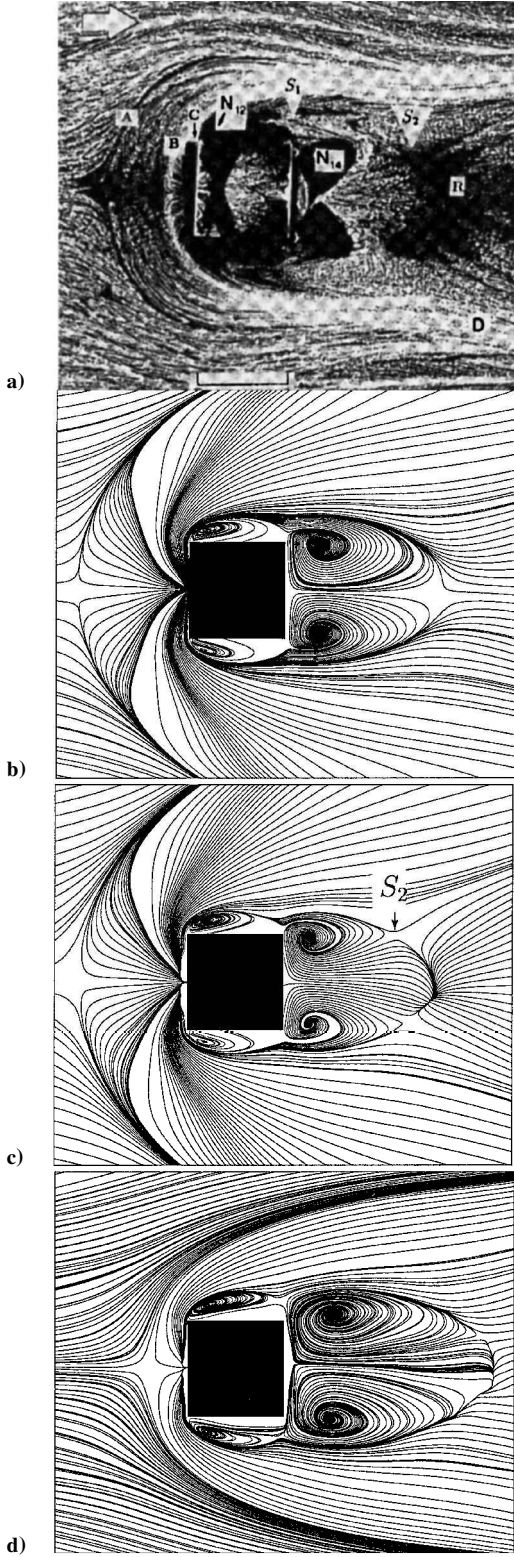


Fig. 7 Comparison of a) oil-film visualization by Martinuzzi and Tropea (from Ref. 6 with permission) with streamlines of the mean flow projected onto the channel floor for LES with b) OEM, c) LDKM, and d) without a model.

We visualized the lateral vortices using the second invariant of the velocity gradient Q defined in Ref. 46 and followed their lifespan from the formation close to the front vertical edge of the cube to the breakdown close to the rear vertical edge of the cube. Here, we are limited to showing only some snapshots in Fig. 9, with a fully developed lateral vortex in Fig. 9a and a breakdown of this vortex in Fig. 9b. The lateral vortex is nicely shown in Fig. 9a and has the shape of the ear of a tea cup. At approximately 80% of the

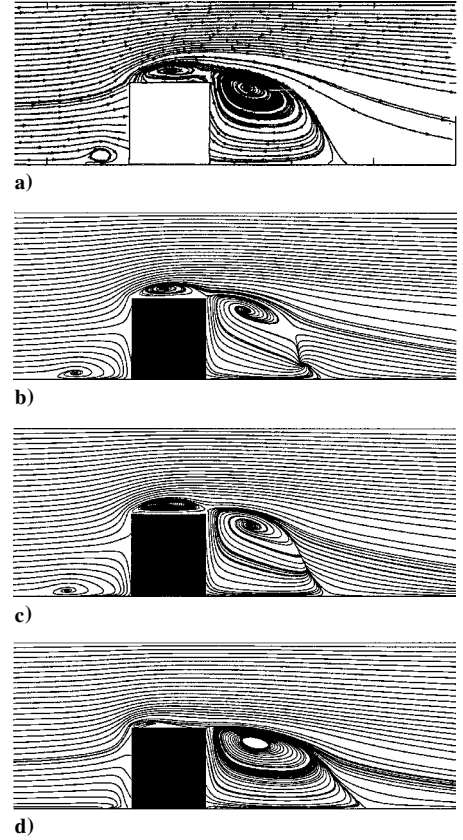


Fig. 8 Streamlines of the mean flow projected onto the center plane of the cube using a) experiment⁶ (from Ref. 45 with permission), b) LDKM, c) OEM, and d) NOM.

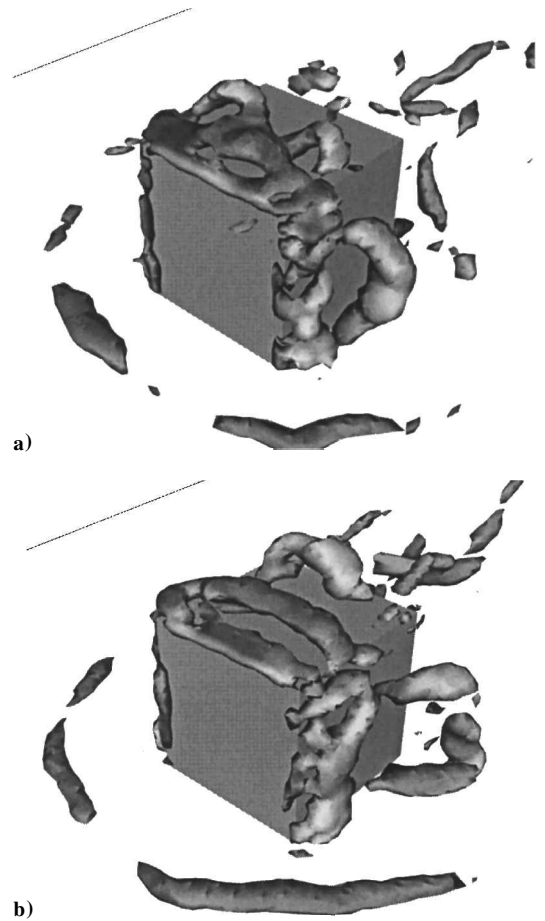


Fig. 9 Instantaneous second invariant of the velocity gradient $Q=5$.

cube height (the tea cup), the vortex (the ear) attaches to the lateral side of the cube. The lateral vortex can also be seen in Fig. 6. There are two primary flow states characterized by different positions of the horseshoe vortex (Fig. 9). The probability density function (PDF) of drag shows two peaks corresponding to these two flow states (not shown in the paper). Similar observation is made in the LES by Shah and Ferziger.⁷ We also found a distinct bimodal form of the PDF of the velocity distribution in the region between curves A and B in Fig 7a. This agrees with LES results in Ref. 7 and experimental findings by Larousse et al.⁴

Conclusions

LES was used to simulate the flow around a three-dimensional bluff body. This flow was studied thoroughly, both in the mean and instantaneously. The inlet boundary condition was the experimental velocity profile constant in time. This together with an insufficiently fine resolution of the boundary layer unavoidably leads to an incorrect boundary-layer thickness upstream of the body. Still, the sharp edges of the body define the separations and minimize the influence of the inlet boundary condition on the statistics.

It was shown that it is possible to obtain accurate results at an acceptable computational cost. The computational cost for the case of the surface-mounted cube is represented by ~ 60 CPU h on an SGI R10000. Two one-equation subgrid models were compared. Although the two models gave similar results, there are some differences. The LDKM is more local, and results for the statistics are slightly better than with the OEM (Fig. 3). The topology of the flow predicted with the LDKM is somewhat closer to that in the flow visualization compared to the OEM. The saddle points on the channel floor along the reattachment line (S_2 in Fig. 7c) were predicted with the LDKM, whereas the OEM failed to do so. Both models were able to predict separation and reattachment lengths in good agreement with experiments and previous LES.⁷⁻⁹ The OEM gives a shedding frequency of the side force that is in slightly better agreement with experiments than the LDKM. Flow features observed in the visualization by Martinuzzi and Tropea⁵ are found in simulations using both models. Computations with a model gave considerably better results than computation without a model. The transfer of the turbulent energy was studied, and the reverse transfer of energy (backscatter) was predicted. Finally, we conclude that the LES proposed in this paper using simple inlet boundary conditions, a relatively coarse grid, and a one-equation model gives accurate results.

Acknowledgments

This work was supported by the National Swedish Board for Technical Development and the Volvo Car Corporation. Computer time on the SGI ORIGIN 2000 machines provided by Unix Numeric Intensive Calculations at Chalmers is gratefully acknowledged.

References

- ¹Castro, I. P., and Robins, A. G., "The Flow Around a Surface-Mounted Cube in Uniform and Turbulent Stream," *Journal of Fluid Mechanics*, Vol. 79, Feb. 1977, pp. 307-335.
- ²Hunt, J. C. R., Abell, C. J., Peterka, J. A., and Woo, H., "Kinematical Studies of the Flows Around Free or Surface-Mounted Obstacles; Applying Topology to Flow Visualization," *Journal of Fluid Mechanics*, Vol. 86, July 1978, pp. 179-200.
- ³Schofield, W. H., and Logan, E., "Turbulent Shear Flow over Surface Mounted Obstacles," *Journal of Fluids Engineering*, Vol. 112, No. 4, 1990, pp. 376-385.
- ⁴Larousse, A., Martinuzzi, R., and Tropea, C., "Flow Around Surface-Mounted, Three-Dimensional Obstacles," *9th International Symposium on Turbulent Shear Flow*, Springer-Verlag, 1991, pp. 127-139.
- ⁵Martinuzzi, R., and Tropea, C., "The Flow Around Surface-Mounted Prismatic Obstacles Placed in a Fully Developed Channel Flow," *Journal of Fluids Engineering*, Vol. 115, No. 1, 1993, pp. 85-91.
- ⁶Hussein, H., and Martinuzzi, R. J., "Energy Balance for Turbulent Flow Around a Surface Mounted Cube Placed in a Channel," *Physics of Fluids*, Vol. 8, No. 3, 1996, pp. 764-780.
- ⁷Shah, K. B., and Ferziger, J. H., "A Fluid Mechanics View of Wind Engineering: Large Eddy Simulation of Flow past a Cubic Obstacle," *Journal of Wind Engineering and Industrial Aerodynamics*, Vol. 67, April 1997, pp. 211-224.

- ⁸Hanjalić, K., and Obi, S. (eds.), *ERCOFTAC/IAHR/COST Workshop on Refined Flow Modeling*, Delft Univ. of Technology, Delft, The Netherlands, 1997, pp. 131-225.
- ⁹Rodi, W., Ferziger, J. H., Breuer, M., and Pourquié, M. (eds.), *Workshop on LES of Flows Past Bluff Bodies*, Rotach-Egern, Germany, 1995.
- ¹⁰Spalart, P. R., "Strategies for Turbulence Modelling and Simulations," *International Journal of Heat and Fluid Flow*, Vol. 21, No. 3, 2000, pp. 252-263.
- ¹¹Iaccarino, G., and Durbin, P., "Unsteady 3D RANS Simulations Using the v^2-f Model," *Annual Research Briefs 2000*, Center for Turbulence Research, Stanford Univ., Stanford, CA, 2000, pp. 263-269.
- ¹²Balaras, E., Benocci, C., and Piomelli, U., "Two-Layer Approximate Boundary Conditions for Large-Eddy Simulations," *AIAA Journal*, Vol. 34, No. 6, 1996, pp. 1111-1119.
- ¹³Davidson, L., "Hybrid LES-RANS: A Combination of a One-Equation SGS Model and a $k-\omega$ Model for Predicting Recirculating Flows," *ECCOMAS CFD Conference [CD-ROM]*, Swansea, England, U.K., 2001.
- ¹⁴Spalart, P. R., Jou, W. H., Strelets, M., and Allmaras, S. R., "Detached-Eddy Simulation of an Airfoil at High Angle of Attack," *Advances in DNS/LES, Proceedings of the First AFOSR International Conference on DNS/LES*, 1997.
- ¹⁵Speziale, C. G., "Turbulence Modeling for Time-Dependent RANS and VLES: A Review," *AIAA Journal*, Vol. 36, No. 2, 1998, pp. 173-184.
- ¹⁶Woodruff, S. L., Seiner, J. M., and Hussaini, M. Y., "Grid-Size Dependence in the Large-Eddy Simulation of Kolmogorov Flow," *AIAA Journal*, Vol. 38, No. 4, 2000, pp. 600-604.
- ¹⁷Smagorinsky, J., "General Circulation Experiments with the Primitive Equations," *Monthly Weather Review*, Vol. 91, No. 3, 1963, pp. 99-165.
- ¹⁸Germano, M., Piomelli, U., Moin, P., and Cabot, W., "A Dynamic Subgrid-Scale Eddy Viscosity Model," *Physics of Fluids*, Vol. 3, No. 7, 1991, pp. 1760-1765.
- ¹⁹Lilly, D., "A Proposed Modification of the Germano Subgrid-Scale Closure Method," *Physics of Fluids*, Vol. 4, No. 3, 1992, pp. 633-635.
- ²⁰Schumann, U., "Subgrid Scale Model for Finite Difference Simulations of Turbulent Flows in Plane Channels and Annuli," *Journal of Computational Physics*, Vol. 18, 1975, pp. 376-404.
- ²¹Krajnović, S., and Davidson, L., "Large-Eddy Simulation of the Flow Around a Ground Vehicle Body," Society of Automotive Engineers, SAE Paper 2001-01-0702, 2001.
- ²²Krajnović, S., and Davidson, L., "Large Eddy Simulations of the Flow Around a Simplified Bus," *3rd AFOSR International Conference on DNS and LES*, Arlington, TX, 2001.
- ²³Davidson, L., "LES of Recirculating Flow Without any Homogeneous Direction: A Dynamic One-Equation Subgrid Model," *2nd International Symposium on Turbulence Heat and Mass Transfer*, Delft Univ. Press, Delft, The Netherlands, 1997, pp. 481-490.
- ²⁴Emvin, P., "The Full Multigrid Method Applied to Turbulent Flow in Ventilated Enclosures Using Structured and Unstructured Grids," Ph.D. Dissertation, Dept. of Thermo and Fluid Dynamics, Chalmers Univ. of Technology, Gothenburg, Sweden, 1997.
- ²⁵Rhie, C., and Chow, W., "Numerical Study of the Turbulent Flow past an Airfoil with Trailing-Edge Separation," *AIAA Journal*, Vol. 21, No. 11, 1983, pp. 1525-1532.
- ²⁶Zang, Y., Street, R., and Koseff, J., "A Dynamic Mixed Subgrid-Scale Model and Its Application to Turbulent Recirculating Flows," *Physics of Fluids*, Vol. 5, No. 12, 1993, pp. 3186-3196.
- ²⁷Ghosal, S., and Moin, P., "The Basic Equations for the Large Eddy Simulation of Turbulent Flows in Complex Geometry," *Journal of Computational Physics*, Vol. 118, No. 1, 1995, pp. 24-37.
- ²⁸Davidson, L., "Large Eddy Simulation: A Dynamic One-Equation Subgrid Model for Three-Dimensional Recirculating Flow," *11th International Symposium on Turbulent Shear Flow*, Vol. 3, 1997, pp. 26.1-26.6.
- ²⁹Krajnović, S., and Davidson, L., "Large-Eddy Simulation of the Flow Around a Surface-Mounted Cube Using a Dynamic One-Equation Subgrid Model," *First International Symposium on Turbulence and Shear Flow Phenomena*, edited by S. Banerjee and J. Eaton, Begell House, New York, 1999, pp. 741-746.
- ³⁰Sohankar, A., Davidson, L., and Norberg, C., "Large Eddy Simulation of Flow past a Square Cylinder: Comparison of Different Subgrid Scale Models," *Journal of Fluids Engineering*, Vol. 122, No. 1, 2000, pp. 39-47.
- ³¹Sohankar, A., Davidson, L., and Norberg, C., "Erratum," *Journal of Fluids Engineering*, Vol. 122, No. 3, 2000, p. 643.
- ³²Menon, S., and Kim, W.-W., "High Reynolds Number Flow Simulations Using the Localized Dynamic Subgrid-Scale Model," AIAA Paper 96-0425, 1996.
- ³³Sohankar, A., "Numerical Investigation of Vortex Shedding Around Square Cylinders at Low Reynolds Number," Ph.D. Dissertation, Dept. of Thermo and Fluid Dynamics, Chalmers Univ. of Technology, Gothenburg, Sweden, 1998.
- ³⁴Krajnović, S., and Davidson, L., "Large Eddy Simulation of the Flow Around a Three-Dimensional Bluff Body," AIAA Paper 2001-0432, 2001.

³⁵Krajnović, S., "Large Eddy Simulation of the Flow Around a Three-Dimensional Bluff Body," Thesis for Licentiate of Engineering 00/1, Dept. of Thermo and Fluid Dynamics, Chalmers Univ. of Technology, Gothenburg, Sweden, Jan. 2000.

³⁶Sohankar, A., Norberg, C., and Davidson, L., "Simulation of Unsteady Three-Dimensional Flow Around a Square Cylinder at Moderate Reynolds Numbers," *Physics of Fluids*, Vol. 11, No. 2, 1999, pp. 288–306.

³⁷Breuer, M., "A Challenging Test Case for the Large Eddy Simulation: High Reynolds Number Circular Cylinder Flow," *International Journal of Heat and Fluid Flow*, Vol. 21, No. 5, 2000, pp. 648–654.

³⁸Piomelli, U., Cabot, W., Moin, P., and Lee, S., "Subgrid-Scale Backscatter in Turbulent and Transitional Flows," *Physics of Fluids*, Vol. 3, No. 7, 1991, pp. 1766–1771.

³⁹Domaradzki, J. A., Liu, W., Härtel, C., and Kleiser, L., "Energy Transfer in Numerically Simulated Wall-Bounded Turbulent Flows," *Physics of Fluids*, Vol. 6, No. 4, 1994, pp. 1583–1599.

⁴⁰Vreman, B., Geurts, B., and Kuerten, H., "On the Formulation of the Dynamic Mixed Subgrid-Scale Model," *Physics of Fluids A*, Vol. 6, No. 12, 1994, pp. 4057–4059.

⁴¹Ghosal, S., Lund, T., Moin, P., and Akselvoll, K., "A Dynamic Localization Model for Large-Eddy Simulation of Turbulent Flows," *Journal of Fluid Mechanics*, Vol. 286, March 1995, pp. 229–255.

⁴²Carati, D., Ghosal, S., and Moin, P., "On the Representation of Backscatter in Dynamic Localization Models," *Physics of Fluids*, Vol. 7, No. 3, 1995, pp. 606–616.

⁴³Domaradzki, J. A., and Saiki, E. M., "Backscatter Models for Large-Eddy Simulations," *Theoretical and Computational Fluid Dynamics*, Vol. 9, No. 2, 1997, pp. 75–83.

⁴⁴Sujudi, D., and Haimes, R., "Identification of Swirling Flow in 3-D Vector Fields," AIAA Paper 95-1715, 1995.

⁴⁵Rodi, W., Ferziger, J., Breuer, M., and Pourquié, M., "Status of Large-Eddy Simulations: Results of a Workshop," *Journal of Fluids Engineering*, No. 2, 1997, pp. 248–262.

⁴⁶Jeong, J., and Hussain, F., "On the Identification of a Vortex," *Journal of Fluid Mechanics*, Vol. 285, Feb. 1995, pp. 69–94.

P. Givi
Associate Editor